The Subthermocline Lens D1. Part II: Kinematics and Dynamics*

B. A. ELLIOTT

Cooperative Institute for Marine and Atmospheric Studies, University of Miami, Miami, FL 33149

T. B. SANFORD

Applied Physics Laboratory and School of Oceanography, College of Ocean and Fishery Sciences, University of Washington, Seattle, WA 98105

(Manuscript received 24 September 1984, in final form 24 May 1985)

ABSTRACT

The dynamics of a subthermocline lens observed during the POLYMODE Local Dynamics Experiment are examined using density data and measurements of the velocity field obtained by an absolute velocity profiler. It is shown that the momentum balance is nonlinear. The lens' potential vorticity contours are closed in the horizontal and vertical, trapping low-salinity water at the lens core. The lens's dynamics are explained by a series of elementary models based on the classical Bessel-function vortex. The models show that nonlinearity enters in two ways, through the nonlinear momentum balance and through the finite character of the stretching vorticity. The models suggest a lens anatomy: the core; a boundary layer at the velocity maximum; a buffer zone; and a geostrophic region. The first two terms are self-explanatory. The buffer zone extends from the velocity maximum to a radius we term the geostrophic radius, at which there is a salinity front. On either side of this front the character of the mixing processes is quite different. At larger radii the momentum balance is geostrophic, and the lens remains a coherent structure through finite stretching vorticity.

1. Introduction

One of the more remarkable results of the POLYMODE Local Dynamics Experiment (LDE) is the discovery of a large number of small intense vortices (for an overview of the results of the LDE see McWilliams et al., 1983). Typically their radii are on the order of 15 km, small in comparison to the mesoscale. Furthermore, most are self-compensating; i.e., they have no surface expression, and their signature in the water property data is distinctly different from that of the surrounding fluid. (Lindstrom and Taft, 1986, discuss the statistics of outliers in the water property data in the LDE dataset.) Several case studies are presented from the LDE dataset (Riser et al., 1986; Lindstrom et al., 1986; Elliott and Sanford, 1986). McWilliams (1985) reviews the dynamics and possible formation mechanisms. Elliott and Sanford (1986, hereafter referred to as Part I) examine one of the vortices—referred to as the subthermocline lens D1—and present the data and the techniques used to isolate the vortex from the surrounding flow field. They describe the vortex in terms of water properties, the velocity field, and the region of origin. This study is a sequel to Part I and concentrates on D1's dynamics.

In the next section we briefly describe the data utilized by this study. The reader should consult Part I for a more complete description of the dataset and analysis techniques. A test of the gradient wind balance made in Section 3 confirms that the centripetal acceleration is a critical term in the momentum balance. Using velocity measurements from an absolute velocity profiler (AVP) developed by Sanford et al. (1985) and the density field resolved by the CTD survey, a section of potential vorticity is presented in Section 4. It shows that the low-salinity water of the vortex is trapped by closed potential vorticity contours. The radial structure of the potential vorticity at the lens's mid-depth is examined in detail. Among other things, we find a boundary layer at the velocity maximum. A salinity front exists farther out along the radius.

To understand the structure of the lens in the potential vorticity field, a series of elementary models is developed (Section 5). For the structure outside the velocity maximum, three models are presented, in descending complexity: the first is distinguished by being based on a nonlinear momentum balance and having finite stretching vorticity; the geostrophic momentum balance with finite stretching vorticity characterizes the second; and the third model is based on the formulation for quasi-geostrophic potential vorticity. For the structure inside the velocity maximum, two models are presented: the first is based on vorticity dynamics, whereas the second assumes that the mass field adjusts to the curvature vorticity (v/r) in a manner analogous to the way the mass field of a zonal current adjusts to a vari-

* POLYMODE Contribution Number 183.

able coriolis parameter. Hence, the curvature vorticity is treated as a proxy beta effect. The discussion presented in the last section focuses on questions not fully answered by our analysis.

2. Data

Lens D1 was moving to the SW at speeds greater than 20 cm s^{-1}. Let V_B be the velocity of the background, large-scale flow advecting D1 through the survey region. This velocity is used as a reference for a moving coordinate system. The coordinates relative to the eddy's center are determined for each measurement, and the measurements are composited at the reference time (t_0), chosen to be the time of the measurement closest to the eddy's center. A detailed discussion of the methodology is given in Part I. Figure 1 shows the sampling pattern in the moving coordinate system for the data of fine-scale survey 3 (FS3). Similar plots for FS1 and FS2 are given in Part I.

Shown in Fig. 1 are the positions of 13 absolute velocity profiler (AVP) drops. We have subtracted from each of the profiles in the eddy a background profile and the vertically averaged velocity below 3000 db. The rationale for using this procedure is discussed in Part I.

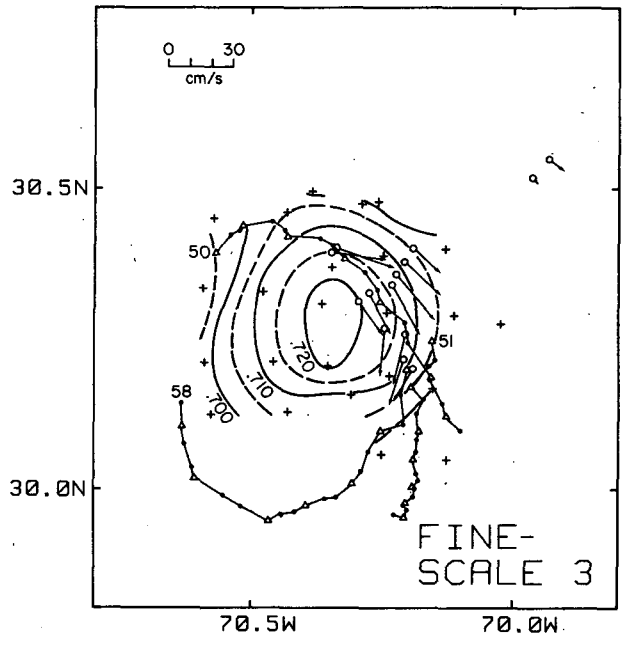

FIG. 1. Map of the geopotential anomaly in dynamic meters (dyn m) at 1500 db relative to 3000 db in the advected coordinate system for fine-scale survey 3. The reference velocity is 13.9 cm s^{-1} at 219°T. The positions of the displaced CTD stations are represented by plus signs. The positions of AVP drops are plotted as open circles. The AVP velocity vectors are the difference between the observation and the reference velocity profile, with the vertically averaged residual below 3000 db subtracted. See Part I for a discussion of the methodology and for similar plots for fine-scale surveys 1 and 2. The line of AVP stations running from SW to NE is section 1; the line running roughly SE to NW is section 2. Also plotted are tracks (lines with triangles) of three SOFAR floats (see Part I for further discussion).

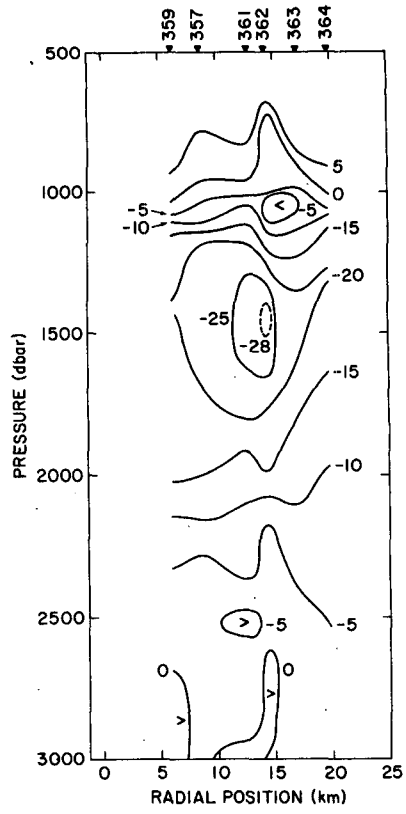

FIG. 2. Azimuthal velocity component for section 1. Contours have not been extended above ~900 db.

Two radial sections of velocity are present. Section 1 consists of six AVP drops running roughly SW to NE, radially from 6 to 20 km. Contoured values of the azimuthal velocity component are presented in Fig. 2. Values shallower than 1000 db are not considered an accurate representation of the structure of the flow field because of shear in the background flow (discussed in Part I). Section 2 runs radially from 10 to 17 km, roughly SE to NW. The profiles of section 2 are presented and discussed in Part I. We will not discuss them here. However, calculations identical to those performed on the velocity of section 1 have also been made on the data of section 2. The azimuthal velocity section, Fig. 2, shows a jetlike core from about 1300–1600 db, 14 km from the eddy's center. The maximum observed azimuthal component is 28.6 cm s^{-1} at about 1500 db at drop 362. Outside the high velocity core the azimuthal component decays exponentially along the 1500-db surface (Part I). Inside the velocity maximum the velocity behaves similarly to the radial derivative of a Gaussian function.

To examine the balance of terms in the momentum equation and to compute a vertical section of potential vorticity, the water property data for each of the fine-scale datasets are azimuthally averaged. The resulting averaged density and salinity sections for FS3 are presented in Figs. 3a and 3b respectively. The eddy is a

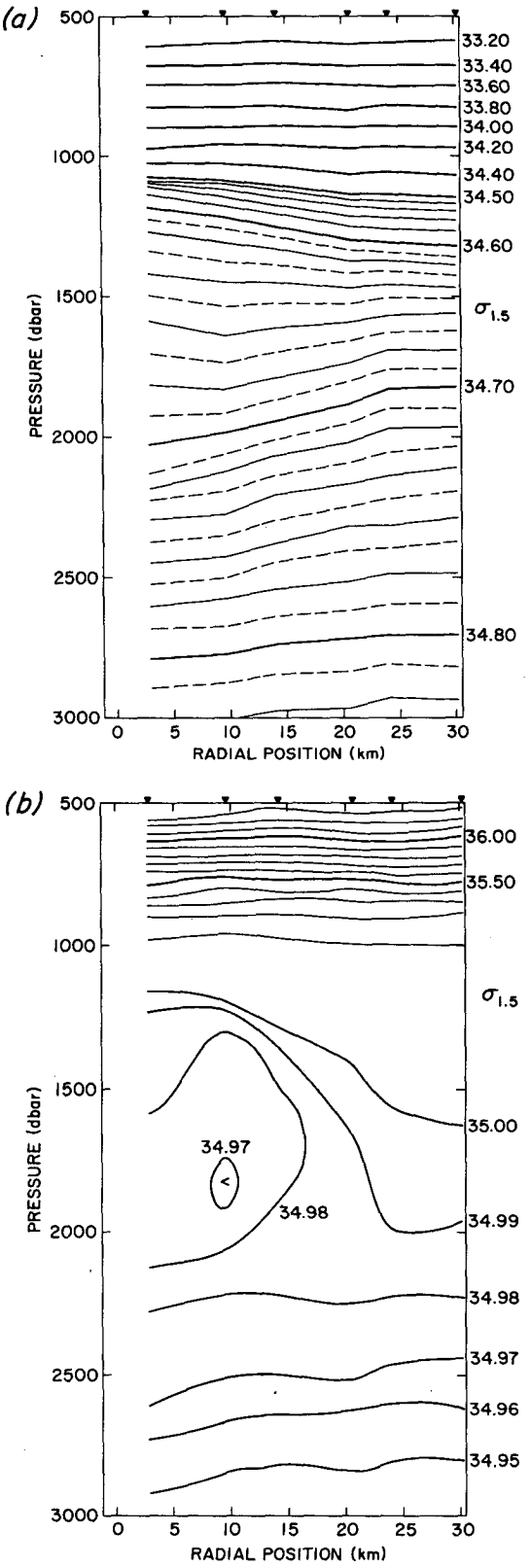

FIG. 3. (a) Azimuthally averaged section of potential density anomaly relative to 1500 db ($\sigma_{1.5}$) for fine-scale survey 3. (b) Azimuthally averaged section of salinity for fine-scale survey 3. [In (a) and (b), solid triangles denote locations of average stations.]

low-salinity lens centered at about the 34.65 $\sigma_{1.5}$ surface, or about 1500 db. Above, the density surfaces are perturbed upward to about 1000 db. Below, downward perturbation of the density surfaces extends to 3000 db. In the radial direction, the lens's effect is present throughout the section. The doming of the 35.00 and 34.99‰ isohalines indicates the lens's salinity signal extends radially to at least 25 km. See Part I for a complete discussion of the structure of this lens in the density and water property data.

3. Test of the gradient wind balance

The momentum balance in the radial direction is

$$-fv^* - \frac{v^{*2}}{R} = -\frac{1}{\rho}\frac{\partial P}{\partial R} \cdots, \tag{3.1}$$

where f is the Coriolis parameter, v^* the azimuthal velocity, ρ the density, P the pressure, R the radial coordinate, and the ellipses denote the higher-order terms.[1] The Rossby number ($\epsilon = v_m/fR_m$, where v_m is the maximum azimuthal velocity and R_m is its radial coordinate) at the high velocity core is 0.27, hence the cyclostrophic term should be an important component of the momentum balance. To test this hypothesis, the azimuthal velocity computed from the density data is compared with the AVP values.

The geostrophic velocity is

$$v_g^* = \frac{1}{f}\frac{\partial \Delta\phi}{\partial R}, \tag{3.2}$$

where $\Delta\phi$ is the geopotential anomaly relative to 3000 db. The gradient wind balance is

$$v^* + \frac{v^{*2}}{fR} = \frac{1}{f}\frac{\partial \Delta\phi}{\partial R}. \tag{3.3}$$

To determine v_g^* and v^*, an empirical model

$$\Delta\phi = \Delta\phi_B + a\exp(-bR^2) \tag{3.4}$$

is fit to the radial distribution of the geopotential anomaly at 1500 db. On the right side of (3.4), $\Delta\phi_B$ is the geopotential anomaly of the far field; a and b are the coefficients of the fit. The points used in the fit, the coefficients, and a plot of the resulting empirical curve are shown in Fig. 4. The geostrophic velocity is obtained by differentiating (3.4) with respect to R and solving for v_g^* using the Coriolis parameter at the latitude of the lens's center. Geostrophic velocities are computed at the radial position of each AVP station. Estimates of the gradient wind velocity are made at each AVP station by solving (3.3) for v^*. The results are plotted in Fig. 5.

The solid line in Fig. 5 represents a one-to-one correspondence between the velocity computed from the

[1] Throughout the text we will use an asterisk to denote a dimensional quantity when we believe there is the potential for confusion.

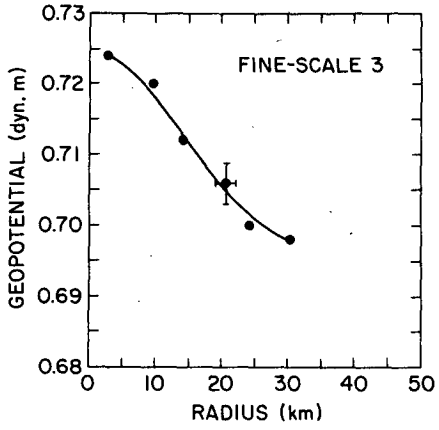

FIG. 4. Azimuthally averaged geopotential anomaly of 1500 db relative to 3000 db for fine-scale survey 3. Error bars are rms values from the azimuthally averaged data. Also shown is the empirical model given in the text: $\Delta\phi_B = 0.695$ dyn m; $a = 0.030$ dyn m; and $b = 26.4 \times 10^{-4}$ km^{-2}.

density data and that measured by the AVP. The remaining two lines represent models of the form

$$Y = A \cdot V_{\mathrm{AVP}},$$

where Y is either v^* or v_g^*, V_{AVP} is the measured velocity, and A is the slope of the regression line (given in the figure caption). The scatter about each model is ± 1.8 and ± 2.2 cm s^{-1} for the geostrophic and gradient wind velocities, respectively.

The computed gradient wind velocities underestimate the measured values owing to smoothing by the model (3.4). The slope of the regression line for the geostrophic data is significantly different from one and is also significantly different from that for the gradient wind velocities. The slope of the regression line for the gradient wind velocities is not significantly different from one. Consequently, the momentum balance is predominately a gradient wind one. We cannot resolve the higher-order terms in (3.1).

4. Vorticity

The AVP profiles provide a unique opportunity to describe the structure of the lens's vorticity field independent of any dynamical assumptions about the momentum balance. Using the data, order-of-magnitude estimates show that the potential vorticity (Ertel, 1942) can be expressed as

$$q^* = \frac{1}{\rho}\frac{\partial v^*}{\partial z}\frac{\partial \rho}{\partial R} - \frac{1}{\rho}\left(\frac{\partial v^*}{\partial R} + \frac{v^*}{R} + f\right)\frac{\partial \rho}{\partial z}, \quad (4.1)$$

where the largest source of error (at times, 10% of the vertical component) enters through neglecting the azimuthal gradient of the radial velocity in the term for the vertical component of absolute vorticity.

a. Vertical sections

Each of the velocity derivatives in (4.1) is computed using sections of azimuthal velocity from the AVP data. Density gradients in the R–z plane are derived from the azimuthally averaged CTD data (Fig. 3a) and interpolated by cubic splines to the position of the vorticity calculations. The contoured potential vorticity is presented in Fig. 6, based on the velocity data of Fig. 2.

Over the section the contribution to the potential vorticity by the first term on the right side of (4.1) is typically 10–15% of the values plotted in Fig. 6. At the lens's mid-depth this term is zero (cf. Fig. 3a). At this same depth the potential vorticity is a minimum. At shallower depths the large values are due to the vertical density gradient, and similarly for the weak, deeper maximum. The most striking feature in this section is the minimum in the potential vorticity at the lens's mid-depth. Setting the boundaries of this minimum at the 1×10^{-13} cm^{-1} s^{-1} contour, the section indicates that at about 1600 db this contour must close farther out along the radius.

In an inviscid fluid both the potential vorticity and the potential density are conservative scalar properties of a fluid parcel. Hence, fluid parcels are constrained to move along the space curves defined by the intersection of constant q^* surfaces and constant ρ surfaces. A comparison of Figs. 3a and 6 clearly shows the intersection fields of q^* and ρ, indicating that the dynamics of the lens's closed circulation traps fluid at the

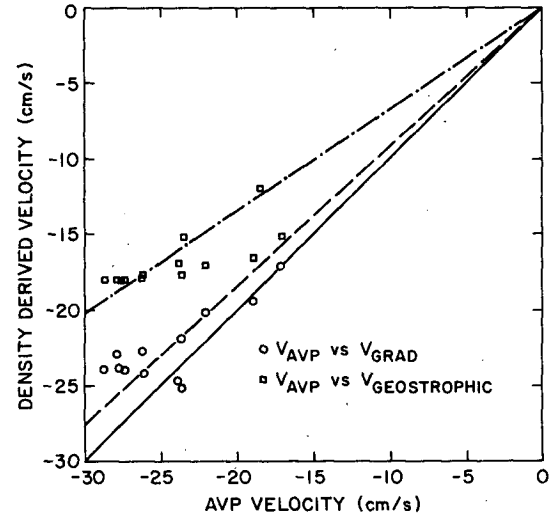

FIG. 5. Scatter plot of the azimuthal velocity at 1500 db for the fine-scale 3 data. The abscissa represents the AVP measured values. The ordinate represents the geostrophic and gradient wind velocities (at the same radial positions as the AVP data) computed from a model fit to the geopotential anomaly field at 1500 db relative to 3000 db. The solid line has a slope of 1. The dashed line has a slope of 0.91 and the dash-dot line a slope of 0.61. See text for further explanation.

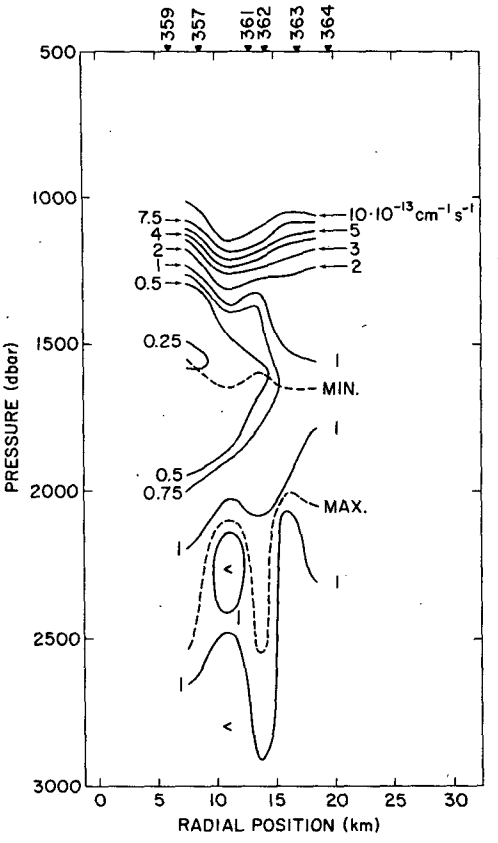

FIG. 6. Section of potential vorticity as computed from the AVP data and the azimuthally averaged density field. Errors are estimated to be about 10% of the observed value.

core of the vortex. This trapping accounts for the maintenance of low-salinity water at the vortex core.

b. *Radial structure*

Since there is a variety of mesoscale rings and eddies having different strengths and scales, we chose to express D1 in nondimensional terms. This representation may aid in comparisons among various eddies. Salinity anomaly (δS^*, to be defined later), Brunt-Väisälä frequency (N^{*2}), absolute vorticity (ω^*) and potential vorticity (q^*) are plotted against radial distance to define the radial structure and scales, and against each other to illustrate more clearly the interrelationships between the different variables. The salinity and Brunt-Väisälä frequency values on the 34.66 $\sigma_{1.5}$ surface are obtained from CTD profiles. The salinity is converted to a salinity anomaly by subtracting it from the salinity at the same density level of the Bryden and Millard (1980) reference profile. Nondimensional plots of N^2 and δS are presented in Figs. 7 and 11 respectively. The nondimensionalizing factor of the salinity anomaly (50 ppm) is roughly the amplitude of the lens's signal on this density surface. The Brunt-Väisälä frequency is nondimensionalized by its far-field value (N_0^2), determined from the reference density profile. The radial coordinate is nondimensionalized by R_m.

Inside $1.5R_m$ the scatter on both plots is what is expected from measurement error. The azimuthal variability in both variables is small, suggesting that the azimuthal variability of the relative vorticity should be small. We assume it to be such, and develop a procedure to estimate the potential vorticity at each CTD station.

At the lens's mid-depth the vertical shear is zero, and (4.1) reduces to

$$q^* = \frac{N^{*2}}{g}\left(\frac{1}{R}\frac{\partial}{\partial R}(Rv^*) + f\right). \tag{4.2}$$

At each CTD station the stratification is computed from the density profile, f is assumed constant, and the relative vorticity is determined from radial fits to the measured azimuthal velocity field. For data inside the velocity maximum the empirical model is the function

$$v = a_1 r \exp[(1 - r^2)/2], \tag{4.3}$$

where $r = R/R_m$ and $v = v^*/v_m$. Outside the velocity maximum the functional

$$v = a_1 \exp[a_3(1 - r)] \tag{4.4}$$

is used. The a_i in the above equations are coefficients of the fits. The two models are matched at the velocity maximum. See Part I for further discussion. Separate model fits are made every 50 db from 1450 to 1650 db. Computed values of ω^* and q^* are interpolated to the 34.64, 34.65, and 34.66 $\sigma_{1.5}$ surfaces. Interpolation errors are inconsequential. Figure 8 presents the nondimensional absolute vorticity (ω^*/f), and Fig. 9 the nondimensional potential vorticity $[q^*/(fN_0^2/g)]$ for the 34.66 $\sigma_{1.5}$ surface. Plots for the other two density surfaces are similar.

Figure 8 shows the empirical model from the fits at 1600 db and the observed values of absolute vorticity on the 34.66 $\sigma_{1.5}$ surface. The observation nearest the

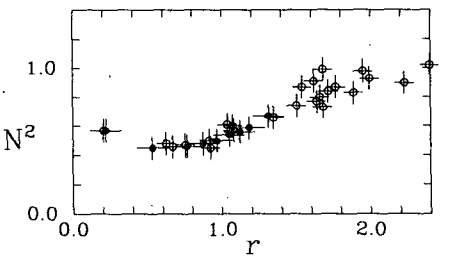

FIG. 7. Scatter plot of the nondimensionalized Brunt-Väisälä frequency squared on the 34.66 $\sigma_{1.5}$ surface versus its nondimensionalized radial distance. The nondimensionalizing factor for the Brunt-Väisälä frequency squared is 1.9×10^{-6} s^{-2}, the far-field value. The error is estimated as $\pm 2 \times 10^{-7}$ s^{-2}. The radial distance is nondimensionalized by the radial distance of the velocity maximum (14.1 km), and the error is ±0.9 km. The open symbols are values at the CTD stations; the solid symbols are values at the AVP stations as interpolated from the azimuthally averaged density data (Fig. 3a).

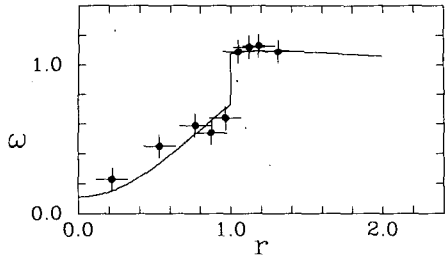

FIG. 8. As in Fig. 7 but for absolute vorticity. The absolute vorticity is nondimensionalized by the Coriolis parameter (7.35×10^{-5} s^{-1} at 30.28°N). The error in relative vorticity is estimated as $\pm 6 \times 10^{-6}$ s^{-1} at 1600 db. The solid symbols are observed values. The solid curve is derived from the empirical fits to the velocity data at 1600 db ($a_1 = 0.99$, $a_3 = 1.29$).

center is based on the assumption that the velocity is zero at the center. The sampling is best near the velocity maximum. It is evident that near the velocity maximum there is an abrupt change in the relative vorticity consistent with the existence of a frontal or boundary layer structure. Inside the velocity maximum the relative vorticity is negative but outside it is positive. In Fig. 9 the solid symbols are observed values of the potential vorticity. Inside the velocity maximum the potential vorticity increases with respect to r. Outside the velocity maximum q again increases in a nearly linear fashion. At the velocity maximum the magnitude of the potential vorticity nearly doubles because of the abrupt increase in the relative vorticity. The scatter in the data points inside 22 km is small; a coherent signal is present. Outside this radius the scatter increases because of an increase in the variability of N^2 (Fig. 7). This is to be expected since the error in the radial coordinate increases radially outward and the lens is interacting with the ambient fluid. At about 35–40 km, the potential vorticity of the lens merges with that of the ambient fluid. The region of trapped fluid extends considerably beyond the velocity maximum.

In Fig. 9, the larger a fluid parcel's potential vorticity the farther out it is along the radius. Therefore we can use q as a coordinate of a fluid parcel along the density

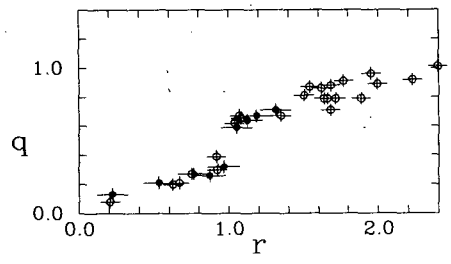

FIG. 9. As in Fig. 8 but for the potential vorticity. The nondimensionalizing factor is 1.42×10^{-13} cm^{-1} s^{-1}, the far-field value. The error is estimated at $\pm 6.0 \times 10^{-15}$ cm^{-1} s^{-1}. The open symbols represent values calculated at CTD stations; the solid symbols are at AVP stations.

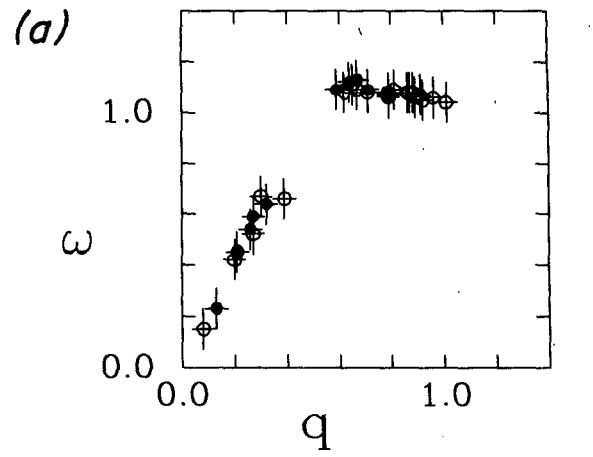

FIG. 10a. Scatter plot of the potential vorticity against the vertical component of absolute vorticity on the 34.66 $\sigma_{1.5}$ surface. Both quantities are nondimensionalized. The nondimensionalizing factor and the estimated error for the potential vorticity are given in the caption of Fig. 9. Solid symbols are values at the AVP stations; open symbols are values at the CTD stations.

surfaces. In Fig. 10a, q is plotted against absolute vorticity, and against N^2 in Fig. 10b. In Fig. 10a, the absolute vorticity is >1 outside the velocity maximum ($q_m = 0.5$) and <1 inside R_m. Hence, at q_m the relative vorticity must be equal to zero and the absolute vorticity must be f. Inside the velocity maximum, q is very nearly a linear function of ω. Outside the velocity maximum, q (Fig. 10b) is nearly a linear function of N^2, but inside it is approximately independent. Then

$$\left.\begin{aligned} \Delta q &= N_m^2 \Delta\omega, \quad r \leqslant 1 \\ \Delta q &= \omega_m \Delta N^2, \quad r \geqslant 1 \end{aligned}\right\}. \tag{4.5}$$

Here N_m^2 is the value of the stratification and ω_m is the absolute vorticity ($\omega_m = 1$) evaluated where the relative vorticity is zero. For $r < 1$, it is the variation in relative

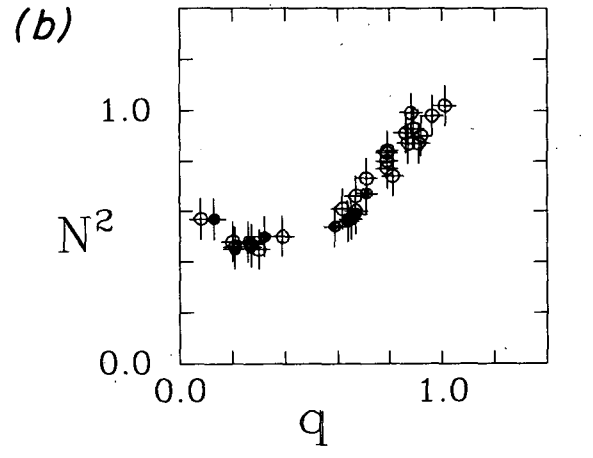

FIG. 10b. As in 10a except against the Brunt-Väisälä frequency squared. The nondimensionalizing factor for the Brunt-Väisälä frequency is given in the caption of Fig. 7, as is the estimated error.

vorticity (f constant) that dominates. For $r > 1$, the variation in q is dominated by the stretching vorticity. The magnitude of q is determined by N_m^2, which in some unknown fashion is determined by the dynamics.

The scatter plot of the radial variation of the salinity anomaly in Fig. 11 shows that at radii larger than about 22 km ($1.5R_m$) the magnitude of the anomaly decreases with increasing r. Inside about 18 km the anomaly is nearly constant. At about 10 km there is a perturbation in the magnitude of the anomaly, where it has values about 20% larger than the measurements on either side. This is the signal of the salinity minimum at 1800 db in the vertical section of Fig. 3b. In Part I, we present maps of the salinity on density surfaces. The maps represent this low-salinity signal as a patch centered on a single CTD station. It could be that it is an annulus of low-salinity water. [An annular structure would imply that the salinity field is well mixed along streamlines (Rhines and Young, 1983).] The data are not sufficient to verify the annular structure.

In Fig. 11 the magnitude of the salinity anomaly decreases by a factor of two outside the radius of the velocity maximum. However, the length scale over which this occurs is ambiguous. The point at $1.3R_m$ is in the southwest quadrant of the lens. A lack of samples in other quadrants precludes our determining whether this point represents an azimuthal perturbation to the salinity field or whether the salinity anomaly of the core extends symmetrically out to this radius. To address this question we compile all the salinity data from the three fine-scale surveys (Figs. 12a, b). Note that this is the first time that we have introduced data from FS1 and FS2. We have avoided doing so because for these two earlier surveys the error in the coordinate systems' reference velocity is estimated to be quite large (Part I). Maps of the geopotential anomaly for FS1 and FS2 suggest large azimuthal perturbations to the lens's current. But it is unclear whether these perturbations are real features of the lens's circulation or are artificially generated by the compositing procedure. Ideally, then, to examine the structure of the salinity anomaly, one would like to plot it against some conservative quantity that is independent of any model of the background flow. The ideal conservative quantity is the potential

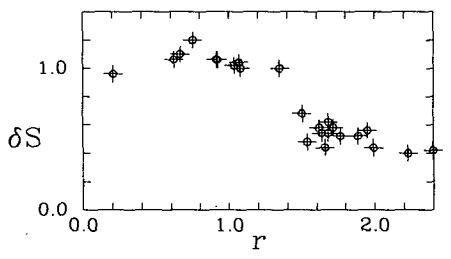

FIG. 11. As in Fig. 7 but for the salinity anomaly. The far-field value of the salinity is 35.028‰. The nondimensionalizing factor is 50 ppm, and the expected error is ±3 ppm.

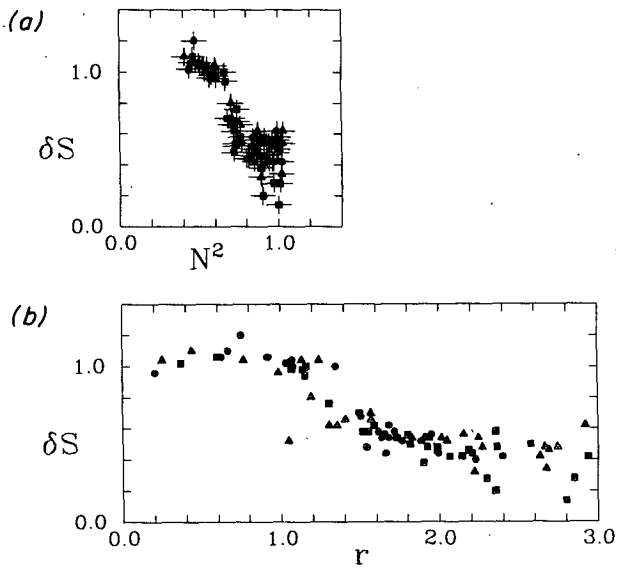

FIG. 12a. Scatter plot of the salinity anomaly against the Brunt-Väisälä frequency squared on the 34.66 $\sigma_{1.5}$ surface for all three fine-scale surveys. Both variables are nondimensionalized—see the captions of Figs. 7 and 11. FS1: squares, FS2: triangles, FS3: circles.

FIG. 12b. As in 12a except against the station's radial coordinate.

vorticity, but its use is precluded because q must be inferred from the data. The Brunt-Väisälä frequency is the next best choice, provided that perturbations to the relative vorticity of the lens's basic current are small. This plot is presented in Fig. 12a.

The data in Fig. 12a fall into two—possibly three—regions: for values of N^2 greater than about $0.8N_0^2$, there is no distinct functional relationship between the salinity anomaly and the stretching vorticity. Note that the salinity anomaly does not converge to 0 as N^2 approaches its far-field value. This may indicate that N_0^2 does not adequately represent the stratification immediately outside the survey area during the time of the lens's passage through the LDE region. Values of the salinity anomaly greater than 0.9 (typical core value) are found at values of N^2 less than $0.7N_0^2$. In between, there is a gap, then a nearly linear relationship between the salinity anomaly and the Brunt-Väisälä frequency as the latter increases. The data plotted against their radial distance (nondimensionalized by the radius of the velocity maximum of FS3) are presented in Fig. 12b. For reasons given above, some of the scatter is artificial. But it is clear that the core values of the salinity anomaly extend out to about $1.3R_m$, after which there is a sharp decrease in the magnitude of the salinity anomaly. Hence there is a salinity front at $1.3R_m$ (18 km) which is displaced radially outward from the velocity maximum and the potential vorticity front in Fig. 9.

Batchelor (1956) showed that at large times and at large Reynolds numbers the circulation inside closed streamlines will approach solid-body rotation in the

limit of small viscosity. The vorticity is homogenized, along with any accompanying scalar fields. Rhines and Young (1983) speculate that such states can occur in isolated vortices. Our data demonstrate that a well mixed scalar field is only a necessary condition for the existence of a homogenized potential vorticity field. Although the stratification and salinity (Figs. 7 and 11) are nearly uniform inside the velocity maximum, the potential vorticity is not. This is illustrated in Fig. 10b, and perhaps even more dramatically by Fig. 13, which shows the salinity to be nearly uniform over a large range of the potential vorticity.

5. Models

The interpretation of the signals given in the previous section is confounded by the nonlinearity of the dynamical balances. We have very little intuition about how the nonlinearity works, and are using models to gain physical insights. Since much of our insight is based on quasi-geostrophic dynamics, we can use that as a frame of reference and anticipate that the nonlinearity will enter in two ways: through the nonlinearity of the momentum balance and through the finite displacements of the density surfaces from their equilibrium positions. In the quasi-geostrophic limit these displacements enter the potential vorticity through the stretching term, which is assumed to be no larger than the Rossby number which is assumed to be small.

We determine nonanalytic equilibrium solutions to an f-plane vortex. Of course the lens exists on the β-plane. In the quasi-geostrophic limit, both analytic (e.g., Flierl, 1979b) and nonanalytic (e.g., Flierl et al., 1980; Berestov, 1979) equilibrium solutions exist. But their parametric range is quite different from that of the lens. Their β-Rossby number ($v_m/\beta R_m^2$) is on the order of 1 or less, whereas that for the lens is on the order of 70 (nearly an order of magnitude larger than that of a Gulf Stream cyclonic ring). Such a large value indicates the β-effect can be neglected.

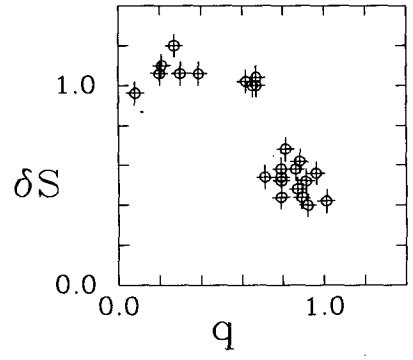

FIG. 13. Scatter plot of the salinity anomaly against the potential vorticity on the 34.66 $\sigma_{1.5}$ surface for the data of FS3. Nondimensionalizing factors and the error estimates are given in the captions of Figs. 9 and 11.

The data justify using nonanalytic solutions. The potential vorticity (Fig. 9) exhibits an abrupt change at the velocity maximum. We can model this region as a boundary layer, but the usefulness of such a model is limited since we do not know the value of the frictional coefficient. Consequently, we simplify the problem by using nonanalytic solutions with a matching condition at the velocity maximum.

The ocean is modeled as a three-layer reduced-gravity system with infinitely deep upper and lower layers. The lens is assumed to be advected through the surrounding fluid by a uniform barotropic flow. Hence we consider the lens's dynamics independent of the large-scale flow field. This is approximately the case because the observed background flow field has weak horizontal ($0.02f$) and vertical (see Part I) shear.

In what follows, $v = v^*/(\Omega R_m)$ is the nondimensional velocity, where $\Omega = f/2$ with f the Coriolis parameter, and $\eta = \eta^*/D$ is the nondimensional form of the deviation of the interface from the undisturbed state D (Fig. 14). The nondimensional radial coordinate is defined as $r = R/R_m$. We assume a function ϕ such that ϕ and r are one-to-one, viz. the inverse

$$r = r(\phi) \tag{5.1}$$

exists over the interval of interest, and that

$$\frac{d\phi}{dr} = v. \tag{5.2}$$

In this notation the nondimensional form of the momentum equation is

$$\left(\frac{1}{2r}\frac{d\phi}{dr} + 1\right)\frac{d\phi}{dr} = \frac{d}{dr}(S^2\eta), \tag{5.3}$$

where $S^2 = g'D/f^2R_m^2$ is the Burger number, and g' is the reduced gravity. Another form of (5.3) is

$$\left[\frac{1}{2r}\frac{d}{dr}\left(r\frac{d\phi}{dr}\right) + 1\right]\frac{d\phi}{dr} = \frac{1}{2}\frac{dH}{dr}, \tag{5.4}$$

where

$$H = S^2\eta + \frac{1}{2}\left(\frac{d\phi}{dr}\right)^2$$

is a Bernoulli function. Using (5.1), (5.3) and (5.4) may be written as

$$\frac{1}{2r}\frac{d\phi}{dr} + 1 = \frac{d}{d\phi}(S^2\eta) \tag{5.5}$$

$$\frac{1}{2r}\frac{d}{dr}\left(r\frac{d\phi}{dr}\right) + 1 = \frac{1}{2}\frac{dH}{d\phi}. \tag{5.6}$$

The nondimensional potential vorticity is

$$q = \left[\frac{1}{2r}\frac{d}{dr}\left(r\frac{d\phi}{dr}\right) + 1\right](1+\eta)^{-1}, \tag{5.7}$$

hence

$$\frac{1}{2r}\frac{d}{dr}\left(r\frac{d\phi}{dr}\right) + 1 = (1+\eta)q. \tag{5.8}$$

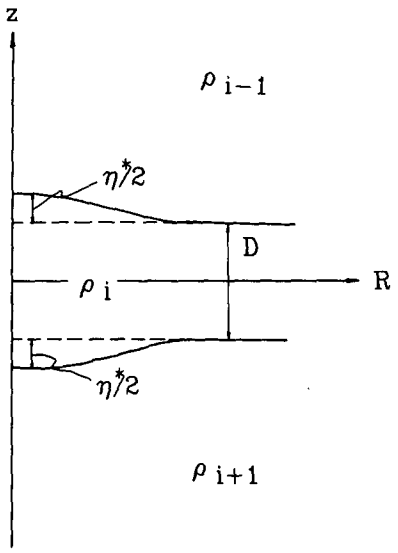

FIG. 14. Sketch of the model coordinate system and parameters.

Comparing (5.6) with (5.8), we use (5.5) to write them more compactly as

$$\frac{1}{2r}\frac{d}{dr}\left(r\frac{d\phi}{dr}\right) + 1 = G(\phi), \tag{5.9}$$

where $G(\phi)$ is as yet some unknown function. We then apply the boundary conditions

$$\begin{aligned} &\phi \to 0, && r \to \infty; \\ &\phi \to \phi_0, && r \to 0; \\ &\frac{d\phi}{dr} \to 0, && r \to \infty; \\ &\frac{d\phi}{dr} = 2\epsilon, && r = 1. \end{aligned} \tag{5.10}$$

These boundary conditions serve to isolate the lens from the surrounding flow field. In so doing we have excluded one common method of solving (5.9), viz., specifying the flow in the far field to obtain an expression for $G(\phi)$.

The model as formulated has three unknown functions—ϕ (or v), η and, say q—and two equations, say (5.3) and (5.7). One method used in the literature to obtain a solution is to specify the potential vorticity to be spatially uniform. Then (5.8) establishes a relation between η and ϕ (or v) which, when combined with the momentum equation (5.3), can be solved for the desired function. Flierl's (1979a) analysis is the most complete, but the same basic approach is used by Csanady (1979), Dugan et al. (1982), and Ikeda (1982). The assumption is untenable in our case.

Since we have direct measurements of the velocity, we can fit those measurements with empirical functions and use (5.2) to solve for ϕ. Usually the results are difficult to interpret, probably because the procedure presumes the measurements are exact. Of course, they are not. The point measurements are imprecise, and there is bias due to the spatial distribution of the sample points. Therefore we search for the simplest mathematical solutions that also explain the data.

a. Solutions outside the velocity maximum

Outside the velocity maximum we assume

$$G(\phi) = \frac{\lambda^2}{2}\phi + b, \tag{5.11}$$

where λ and b are constants.

The solution to (5.9) using (5.11) is

$$\phi = K_0(\lambda r), \tag{5.12a}$$

$$b = 1, \tag{5.12b}$$

where K_0 is the modified Bessel function of the second kind.

To determine λ solve

$$\lambda K_1(\lambda) = 2\epsilon. \tag{5.12c}$$

We must now interpret $G(\phi)$.

If $G(\phi)$ is identified with the right side of (5.6), then the solution is the classical Bessel function vortex. The momentum balance is gradient wind, and the displacement of the interface is finite. Using the expression for the Bernoulli function, we can solve for the interfacial displacement, which can be substituted in (5.7) to obtain the potential vorticity.

As we move outward along the radius we anticipate that the momentum balance becomes geostrophic. Then

$$\eta = \frac{\phi}{S^2}. \tag{5.13}$$

Using the solution (5.12) and (5.13) we can substitute directly into (5.7) and obtain the potential vorticity. But we must check for mathematical consistency. To do so we identify $G(\phi)$ with the right side of (5.8); then, substituting from (5.13), we express the potential vorticity as a power series in ϕ. Hence

$$G(\phi) = \left(1 + \frac{\phi}{S^2}\right)\sum_m^\infty a_m\phi^m; \tag{5.14}$$

or, upon rearranging terms,

$$G(\phi) = a_0 + \left(a_1 + \frac{a_0}{S^2}\right)\phi + \sum_{n=2}^{\infty}\left(a_n + \frac{a_{n-1}}{S^2}\right)\phi^n. \tag{5.15}$$

If this is to be consistent with (5.11), then

$$a_1 = \left(\frac{\lambda^2}{2} - \frac{1}{S^2}\right), \tag{5.16a}$$

$$a_0 = 1, \tag{5.16b}$$

$$a_n = -\frac{a_{n-1}}{S^2}. \tag{5.16c}$$

Equation (5.16) can be solved for a_1; this value can be substituted into the recursion relation (5.16c) to obtain the remaining coefficients. Upon doing so,

$$a_n = (-1)^{n-1}\frac{1}{S^{2n}}\left[\frac{1}{2}(\lambda S)^2 - 1\right], \quad n \geq 1. \tag{5.17}$$

Substituting (5.16b) and (5.17) into the series expansion for potential vorticity, we find it can be simplified using the binomial theorem to

$$q = \left(1 + \frac{\lambda^2}{2}\phi\right)\left(1 + \frac{\phi}{S^2}\right)^{-1}, \tag{5.18}$$

which is precisely (5.7), given the solution (5.12) and the assumption (5.13).

The quasi-geostrophic potential vorticity is defined through a limiting process. As a consequence, the definition of potential vorticity changes from (5.7) to

$$q = \frac{1}{2r}\frac{d}{dr}\left(r\frac{d\phi}{dr}\right) + 1 - \frac{\phi}{S^2}. \tag{5.19}$$

where q is nondimensional. A solution consistent with (5.11) is obtained by neglecting all terms in (5.15) multiplied by ϕ^n, $n > 1$. The solution is (5.16); but, since the potential vorticity is given by (5.19),

$$q = \left(\frac{\lambda^2}{2} - \frac{1}{S^2}\right)\phi + 1. \tag{5.20}$$

Unlike (5.18) the stretching vorticity is assumed to be no greater than the Rossby number, which is itself assumed small ($\ll 1$).

b. *Solutions inside the velocity maximum*

Inside the velocity maximum both forms of nonlinearity are important to the dynamical balances. Consequently, the first solution we present completes the classical Bessel function vortex. Solving (5.9) for

$$G(\phi) = -\frac{\gamma^2}{2}\phi + b', \tag{5.21}$$

then

$$\left.\begin{aligned}\phi &= \phi_0 J_0(\gamma r)\\ b' &= 1\end{aligned}\right\}, \tag{5.22}$$

where γ is determined from the matching condition

$$\gamma\frac{J_1(\gamma)}{J_0(\gamma)} = \lambda\frac{K_1(\lambda)}{K_0(\lambda)}, \tag{5.23a}$$

$$\phi_0 = \frac{K_0(\lambda)}{J_0(\gamma)}. \tag{5.23b}$$

A second, eclectic solution inside the velocity maximum is obtained from (5.5) by assuming

$$2S^2\eta = \frac{1}{2}c_2\phi^2 + c_1\phi + c_0. \tag{5.24}$$

Substituting (5.24) into (5.5) and solving gives

$$\phi = 2\epsilon\exp\left[\frac{1}{2}(1 - r^2)\right] + (c_1 - 2). \tag{5.25}$$

The constant is determined by matching (5.25) with (5.12) at the velocity maximum;

$$c_1 = 2 + K_0(\lambda) - 2\epsilon. \tag{5.26}$$

We include this solution because it explains the data as well as, or better than, the Bessel function solution does; it meets our criterion of mathematical simplicity; and it has a simple physical interpretation. The mass field adjusts to the curvature vorticity (v/r) in a manner analogous to the way the mass field of a zonal current adjusts to the variable Coriolis parameter.

c. *Comparison with the data*

The model solutions depend on two nondimensional parameters, the Rossby number and the Burger number. The former is given by the data. The latter depends on properly calibrating the layered model to the continuously stratified ocean. It is not obvious how to do this since the lens is vertically isolated and a local value of R_d is needed. We consider the Burger number a free parameter and adjust it to enhance the agreement.[2] We define the upper and lower boundaries of the lens as the high-gradient region of the potential vorticity in Fig. 9. Near the lens's center these boundaries coincide with the 34.60 and 34.71 $\sigma_{1.5}$ surfaces. The difference in depth between the two surfaces is defined as the layer thickness of the model. The far-field thickness is determined from the Bryden and Millard (1980) reference profile. The azimuthal velocity is defined as

$$V^* \equiv \left\{\left[\int V^2\left(\frac{N_0}{N}\right)^2 d\rho\right]\left[\int\left(\frac{N_0}{N}\right)^2 d\rho\right]^{-1}\right\}^{1/2}, \tag{5.27}$$

[2] The problem is defining the model interfaces with the upper and lower boundaries of the lens. In the text we use the 34.60 and 34.71 $\sigma_{1.5}$ surfaces. The radius of deformation is $R_d = (N_0 D)/f$, which gives a value of 10 km for these two density surfaces. We actually use 10.5 km—a difference of 5%. In comparing the model potential vorticity with that observed, we use the values of potential vorticity given in Fig. 10. These values are for a single density surface rather than a layer of finite thickness. After adjusting the model to the data by varying the Burger number, we find the latter corresponds to an R_d of 8 km, a value we would obtain by identifying the model interfaces with the 34.60 and 34.70 $\sigma_{1.5}$ surfaces. The adjustments are all reasonable, given the uncertainties. One final point is that Killworth (1983) uses an R_d based on the stratification at the center of the vortex. His approach with our data gives 14.1 km, or a Burger number of 1.

where V denotes the dimensional AVP data. The ratio inside the braces is a measure of the averaged kinetic energy of the fluid parcels between the bounding density surfaces. Using an averaged energy, rather than, say, momentum, assures that the model lens will be mechanically equivalent to the observed lens.

The data, along with the model solutions, are plotted in Figs. 15a, b and 16. Inside the velocity maximum (Fig. 15a), the root-mean-square (rms) difference between the Gaussian model and data (0.9 cm s^{-1}) is smaller than that of the J_0 Bessel function (1.4 cm s^{-1}). However, both are less than the expected measurement error (2.9 cm s^{-1}). Outside the velocity maximum the rms error is 2.0 cm s^{-1}. There is some suggestion that the model solutions decay faster than the observations.

In Fig. 15b, the model solutions are compared with the observed interfacial deviation. Inside the velocity maximum either of the two solutions fits the data. Outside the velocity maximum a difference exists between the solution based on the gradient wind balance in the momentum equation and the two geostrophic solutions. At radii smaller than about $1.3R_m$ the interfacial deviation derived from the geostrophic solutions is larger than that derived using the gradient wind balance. Except for very near the velocity maximum, this difference is not significantly larger than our error bars. At larger radii the solutions are virtually indistinguishable.

As a third point of comparison, the potential vorticity derived from the model solutions is compared with the observed values in Fig. 16. The observed values of potential vorticity are those presented in Fig. 9; the model values are computed with the appropriate Rossby number (0.27). The discontinuity models the sharp change in the potential vorticity in Fig. 9. Inside the velocity maximum the J_0 solution gives a somewhat better fit to the data than the Gaussian solution. Outside the velocity maximum, only the quasi-geostrophic solution is inadequate.

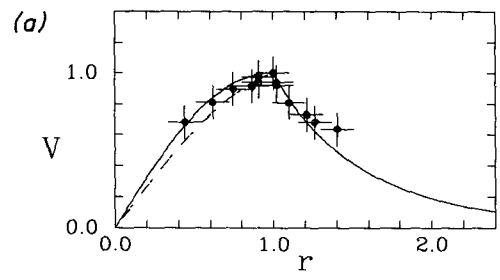

FIG. 15a. Comparison of the model solutions to the measured velocities. The measured velocities are nondimensionalized by the magnitude of the velocity maximum (26.7 cm s^{-1}); the estimated error in the velocity is ±2.9 cm s^{-1}, which includes a systematic (1.5 cm s^{-1}) and random (2.5 cm s^{-1}) component. The radial coordinate is nondimensionalized by the radial distance of the velocity maximum. The estimated error in the radial coordinate of the AVP stations is ±1.5 km. Inside the velocity maximum the dashed line is the J_0 Bessel function solution; the solid line is the Gaussian solution.

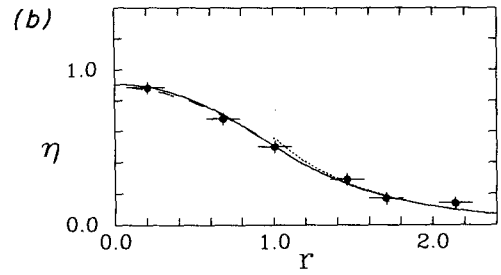

FIG. 15b. Comparison of the observed interfacial deviations to the model solutions. The interfacial deviations are estimated from the azimuthally averaged CTD data by subtracting the thickness of the layer in the far field (504 m) and then nondimensionalizing by the same. The radial coordinate is nondimensionalized by the radial distance of the velocity maximum. Outside the velocity maximum the dashed line represents the solutions obtained assuming a geostrophic momentum balance; inside the velocity maximum the dashed line represents the J_0 Bessel function solution.

The comparisons illustrate the different effects of nonlinearity. For an inviscid fluid the two-dimensional steady state momentum equation is

$$\left(\frac{\zeta}{f}+1\right)f\mathbf{k}\times\mathbf{v}=-\nabla H. \tag{5.28}$$

The momentum balance depends on the local Rossby number (ζ/f). Inside the velocity maximum the magnitude of the local Rossby number is large (>0.27); its sign is negative; and, for a given velocity field, spatial gradients tend to be flattened [the effective value of the Coriolis effect ($\zeta+f$) is reduced]. Outside the velocity maximum the local Rossby number is small (<0.1 at $1.3R_m$) even though the curvature vorticity is still relatively large ($0.2f$ at $1.3R_m$). In this domain the curvature and shear vorticity are of opposite sign and tend to cancel. The momentum balance approaches geostrophy. This is the mechanism by which the momentum at the nonlinear core smoothly merges with the surrounding geostrophic flow.

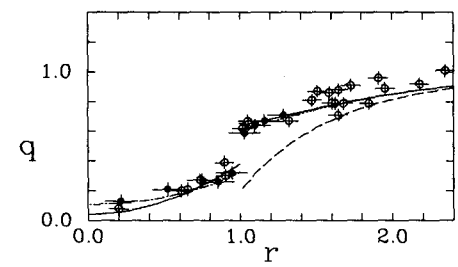

FIG. 16. Comparison of the observed potential vorticity to the model solutions. The potential vorticity values are as given in Fig. 9. Outside the velocity maximum, three solutions are presented: the solid line is the gradient wind solution; the line with short dashes is the geostrophic momentum solution; the line with long dashes is the quasi-geostrophic potential vorticity. Inside the velocity maximum the solid line is the Gaussian solution and the dashed line the J_0 Bessel function solution.

Throughout the domain of the vortex, the stretching vorticity is finite. Outside the velocity maximum it dominates the potential vorticity. The merging of the model solutions in Fig. 15b indicates that at radii larger than $1.3R_m$ the lens's identity is maintained by the stretching vorticity.

Of course, ultimately our interest is in the evolution of features such as this lens, their spindown and interaction with the ambient fluid. This analysis provides guidance for modeling these processes and suggests a lens anatomy: a core that is dominated by the nonlinearity in the momentum equation ($R < R_m$) and a geostrophic regime ($R > 1.3R_m$). At least for this lens, these two regions are separated by a boundary layer at the velocity maximum and a transition or buffer region ($R_m \leq R \leq 1.3R_m$; Fig. 15b) where the nonlinearity in the momentum balance may play a significant role.

6. Discussion

We review briefly: In Section 3 we tested and confirmed the gradient-wind equation, thereby illustrating the importance of nonlinearity in the momentum balance. In Section 4, we described the structure of the lens using the salinity and the potential vorticity. The latter is a dynamic variable and its structure was explained through the use of a series of elementary diagnostic models in Section 5.

The models suggest a lens anatomy: the core; a narrow boundary layer at the velocity maximum; a buffer zone; and the geostrophic region. The boundary between the buffer zone and the geostrophic region occurs at a radius R_g, which we term the geostrophic radius. This boundary is defined by the mergence of two models for the domain outside the core. The two models differ only in the character of the assumed momentum balance, one being geostrophic and the other nonlinear (we need not dwell on the quasi-geostrophic solution). Except, perhaps, very near the velocity maximum, both models fall within our error bars. Hence it is tempting, but ill-advised, to dispense with the difference and refer to the region outside the core as geostrophic. To do so ignores the coincidence of the salinity front and the geostrophic radius.

Compare the signature of mixing processes inside and outside the salinity front. Inside the salinity front the salinity field is nearly uniform. But the lens is not in a homogenized end state (Batchelor, 1956). The fluid parcels are tightly bound to their streamlines. Outside the salinity front the salinity is a mixture of lens and ambient water, the mixing ratio of lens to ambient water increasing inward. In this region the character of the mixing process allows the ambient fluid to penetrate inward toward the vortex core. At the salinity front this process stops or its character changes. There is a strong analogy between flow curvature and stratification (Bradshaw, 1969) such that the former can stabilize flow in a manner quite analogous to the latter. The location of the salinity front at the geostrophic radius (18 km or $1.3R_m$) suggests the nonlinearity in the momentum balance is responsible for the contrasting mixing signatures on either side of the salinity front. A model identifying the mechanism is beyond the scope of this paper.

We have successfully modeled the lens as a classical Bessel function vortex, with the caveat that over the core a Gaussian vortex works equally well. Both models explain the data and both satisfy our criterion of mathematical simplicity. However, this latter criterion makes clear that our approach is essentially subjective. As discussed in Section 5, other models can be developed which will explain as much or more of the variance as those used. In so doing, the mathematical complexity of the problem increases and interpretation becomes more difficult. We have used "Occam's razor" to trim these other models from consideration. But Occam's razor is not an objective criterion. Rather, it clarifies our preconception—viz., that the simplest solutions are best. One needs a well defined theory dealing with the evolution of f-plane vortices to determine whether preconceptions are misconceptions, and such a theory is not available.

The character of the boundary layer at the velocity maximum escapes us. We expect it is a turbulent boundary layer, since the Reynolds number is large. However, it is common to identify the scale of the turbulence with the scale of the boundary layer, and it is not obvious to us that this inference is appropriate. If it is, there should be some indication in the salinity field of either vertical (which we have not shown) or horizontal mixing. If the energy is initially released through pressure work in the form of internal or inertial waves, then one would expect some wave-breaking and, again, evidence of mixing. Examination of Figs. 12a, b does not support this interpretation—at least on the scale of our measurements.

Acknowledgments. Special thanks to C. C. Ebbesmeyer for providing the CTD data, and to J. C. McWilliams and B. A. Taft for cultivating the cooperative spirit exhibited by the LDE group. H. Bryden and R. Millard supplied the processed Bryden-Millard background CTD profiles. C. Stuka of CIMAS typed the manuscript. This paper has benefited from discussions with J. C. McWilliams, C. Rooth, and D. Olson. Support for this work was provided by CIMAS and by NSF Grant OCE-80-00020.

REFERENCES

Batchelor, G. K., 1956: On steady laminar flow with closed streamlines at large Reynolds number. *J. Fluid Mech.*, **1**, 177–190.

Berestov, A. L., 1979: Solitary Rossby waves. *Izv., Atmos. Ocean. Physics*, **15**, 443–447.

Bradshaw, P., 1969: The analogy between streamline curvature and buoyancy in turbulent shear flow. *J. Fluid Mech.*, **36**, 177–191.

Bryden, J., and R. Millard, 1980: Spatially averaged Local Dynamics Experiment CTD stations. *POLYMODE News*, **77** (unpublished manuscript).

Csanady, G. T., 1979: The birth and death of a warm core ring. *J. Geophys. Res.*, **84,** 777–780.

Dugan, J. P., R. P. Mied, P. C. Mignerey and A. F. Schuetz, 1982: Compact, intrathermocline eddies in the Sargasso Sea. *J. Geophys. Res.*, **87,** 385–393.

Elliott, B. A., and T. B. Sanford, 1986: The subthermocline lens D1. Part I: Description of water properties and velocity profiles. *J. Phys. Oceanogr.*, **16,** 532–548.

Ertel, H., 1942: Ein neuer hydrodynamischer Wirbelsatz. *Meteor. Z.*, **59,** 277–281.

Flierl, G. R., 1979a: A simple model for the structure of warm and cold core rings. *J. Geophys. Res.*, **84,** 781–785.

——, 1979b: Baroclinic solitary waves with radial symmetry. *Dyn. Atmos. Oceans,* **3,** 15–38.

——, V. D. Larichev, J. C. McWilliams and G. M. Reznik, 1980: The dynamics of baroclinic and barotropic solitary eddies. *Dyn. Atmos. Oceans,* **5,** 1–41.

Ikeda, M., 1982: A simple model of subsurface mesoscale eddies. *J. Geophys. Res.*, **87,** 7925–7931.

Killworth, P. D., 1983: On the motion of isolated lenses on a beta-plane. *J. Phys. Oceanogr.*, **13,** 368–376.

Lindstrom, E. J., and B. A. Taft, 1986: Statistics of small anomalies in the LDE. *J. Phys. Oceanogr.*, **16,** 613–631.

——, C. C. Ebbesmeyer and W. B. Owens, 1986: Observations of a small cyclonic eddy during the Local Dynamics Experiment. *J. Phys. Oceanogr.*, **16,** 562–570.

McWilliams, J. C., 1985: Sub-mesoscale, coherent vortices in the ocean. *Rev. Geophys.*, **23,** 165–182.

——, and the LDE group, 1983: The local dynamics of eddies in the western North Atlantic. *Eddies in Marine Science,* A. R. Robinson, Ed., Springer-Verlag, 92–113.

Rhines, P. B., and W. R. Young, 1983: How rapidly is a passive scalar mixed within closed streamlines?. *J. Fluid Mech.*, **133,** 133–145.

Riser, S. C., W. B. Owens, H. T. Rossby and C. C. Ebbesmeyer, 1986: The structure, dynamics, and origin of a small-scale lens of water in the western N. Atlantic thermocline. *J. Phys. Oceanogr.*, **16,** 572–590.

Sanford, T. B., R. G. Drever and J. H. Dunlap, 1985: An acoustic Doppler and electromagnetic velocity profiler. *J. Atmos. Oceanic Technol.*, **2,** 110–124.